2011

Solubility of Fe2(OH)3Cl (pure-iron end-member of hibbingite) in NaCl and Na2SO4 brines

Martin Nemer
Sandia National Laboratories (SNL), 4100 National Parks Highway, Carlsbad, NM

Yongliang Xiong
Sandia National Laboratories (SNL), 4100 National Parks Highway, Carlsbad, NM

Ahmed Ismail
Sandia National Laboratories (SNL), 4100 National Parks Highway, Carlsbad, NM

Je-Hun Jang
Sandia National Laboratories (SNL), 4100 National Parks Highway, Carlsbad, NM

Chemical Geology 280 (2011) 26–32

Contents lists available at ScienceDirect

Chemical Geology

journal homepage: www.elsevier.com/locate/chemgeo

Solubility of $Fe_2(OH)_3Cl$ (pure-iron end-member of hibbingite) in NaCl and Na_2SO_4 brines☆

Martin B. Nemer [a,*], Yongliang Xiong [b,*], Ahmed E. Ismail [a,1], Je-Hun Jang [b]

[a] Performance Assessment and Decision Analysis Department, Carlsbad Programs Group, Sandia National Laboratories (SNL), 4100 National Parks Highway, Carlsbad, NM 88220, USA
[b] Repository Performance Department, Carlsbad Programs Group, Sandia National Laboratories (SNL), 4100 National Parks Highway, Carlsbad, NM 88220, USA

ARTICLE INFO

Article history:
Received 14 April 2010
Received in revised form 2 October 2010
Accepted 4 October 2010
Available online 16 November 2010

Editor: J. Fein

Keywords:
$Fe_2(OH)_3Cl$
$Fe(OH)_2$
$GR(II)SO_4$
hibbingite
green rust
Pitzer model

ABSTRACT

Pure-iron end-member hibbingite, $Fe_2(OH)_3Cl(s)$, may be important to geological repositories in salt formations, as it may be a dominant corrosion product of steel waste canisters in an anoxic environment in Na–Cl- and Na–Mg–Cl-dominated brines. In this study, the solubility of $Fe_2(OH)_3Cl(s)$, the pure-iron end-member of hibbingite $(Fe^{II}, Mg)_2(OH)_3Cl(s)$, and $Fe(OH)_2(s)$ in 0.04 m to 6 m NaCl brines has been determined. For the reaction

$$Fe_2(OH)_3Cl(s) + 3H^+ \leftrightarrow 3H_2O + 2Fe^{2+} + Cl^-,$$

the solubility constant of $Fe_2(OH)_3Cl(s)$ at infinite dilution and 25 °C has been found to be $\log_{10} K = 17.12 \pm 0.15$ (95% confidence interval using *F* statistics for 36 data points and 3 parameters). For the reaction

$$Fe(OH)_2(s) + 2H^+ \leftrightarrow 2H_2O + Fe^{2+},$$

the solubility constant of $Fe(OH)_2$ at infinite dilution and 25 °C has been found to be $\log_{10} K = 12.95 \pm 0.13$ (95 % confidence interval using *F* statistics for 36 data points and 3 parameters). For the combined set of solubility data for $Fe_2(OH)_3Cl(s)$ and $Fe(OH)_2(s)$, the Na^+–Fe^{2+} pair Pitzer interaction parameter $\theta_{Na^+/Fe^{2+}}$ has been found to be 0.08 ± 0.03 (95% confidence interval using *F* statistics for 36 data points and 3 parameters). In nearly saturated NaCl brine we observed evidence for the conversion of $Fe(OH)_2(s)$ to $Fe_2(OH)_3Cl(s)$. Additionally, when $Fe_2(OH)_3Cl(s)$ was added to sodium sulfate brines, the formation of green rust(II) sulfate was observed, along with the generation of hydrogen gas. The results presented here provide insight into understanding and modeling the geochemistry and performance assessment of nuclear waste repositories in salt formations.

1. Introduction

When low-carbon steel interacts with chloride-rich anoxic brine, the phase $Fe^{II}_2(OH)_3Cl(s)$, which is the pure-iron end-member of hibbingite $(Fe^{II}, Mg)_2(OH)_3Cl(s)$, is expected to be a likely corrosion product. This phase has been found in the Duluth Complex at Hibbing, Minnesota, USA, with a chemical composition of $(Fe_{1.72}Mg_{0.21}Mn_{0.06}Si_{0.01})_{\Sigma=2.00}[Cl_{0.87}(OH)_{0.12}]_{\Sigma=0.99}(OH)_{3.00}$ (Saini-Eidukat et al., 1994). A hibbingite sample found in a fracture of chalcopyrite and pentlandite from Sudbury, Ontario, Canada, has a composition close to $Fe_{2.00}Cl_{1.06}(OH)_{3.40}$ (Springer, 1989) with Mn and Mg as minor components. In addition to the above occurrences, numerous other natural occurrences of hibbingite as alteration products in meteorites, ancient iron objects, and sulfide ores (e.g. Buchwald and Koch, 1995; Cawthorn et al., 2009; Lee and Bland, 2004; Saini-Eidukat et al., 1998) suggest that hibbingite is a geochemically important, but less recognized, iron-bearing mineral in chloride-rich environments under reducing conditions. Hibbingite is not in any of the thermodynamic databases of the important geochemical codes such as EQ3/6, because of the lack of thermodynamic data.

Just as the composition of hibbingite undergoes variations, there are significant variations in the structure of hibbingite. The formula of hibbingite is simplified as γ-$Fe_2(OH)_3Cl$ in the *Handbook of Mineralogy* (Anthony et al., 2003), whereas others including Buchwald and Koch (1995) identify the β-$Fe_2(OH)_3Cl(s)$ structure as hibbingite, rather than the γ structure. In addition to the β- and γ-$Fe_2(OH)_3Cl(s)$ forms,

☆ Sandia National Laboratories is a multi-program laboratory operated by Sandia Corporation, a wholly owned subsidiary of Lockheed Martin company, for the U.S. Department of Energy's National Nuclear Security Administration under contract DE-AC04-94AL85000. This research is funded by WIPP programs administered by the U.S. Department of Energy.

* Corresponding authors.
E-mail addresses: mbnemer@sandia.gov (M.B. Nemer), yxiong@sandia.gov (Y. Xiong).
[1] Current address: Faculty of Mechanical Engineering, RWTH Aachen University, Schinkelstr. 2, D-52064 Aachen, Germany.

0009-2541/$ – see front matter © 2010 Elsevier B.V. All rights reserved.
doi:10.1016/j.chemgeo.2010.10.003

there is also an α structure found in meteoritic samples (Buchwald and Koch, 1995; Oswald and Feitknecht, 1964). Notably, it is the β-$Fe_2(OH)_3Cl$(s) structure that is predominantly found in the corrosion of man-made iron objects in archaeological discoveries (Reguer et al., 2007). It is difficult to differentiate the β and γ structures, even using techniques such as X-ray diffraction, as many of the peaks belong to both species, and the peaks that are specific to the γ form are either relatively weak compared to the β peaks, or contained in the shoulders of strong β peaks. The structures of the α, β, and γ forms are hexagonal, hexa-rhombohedral, and orthorhombic, respectively (Reguer et al., 2007). Remazeilles and Refait (2008) recently determined the Gibbs free energy of formation for several iron(II) hydroxychlorides, including β-$Fe_2(OH)_3Cl$(s). While a Gibbs free energy was not reported for the γ form, we expect that the Gibbs free energy will be comparable to that of the β-form.

Our motivation for studying the dissolution and precipitation of hibbingite in concentrated brines is to refine our ability to assess the performance of the U.S. Department of Energy's Waste Isolation Pilot Plant (WIPP). The WIPP is a repository for defense-related transuranic waste located in southeast New Mexico at a depth of 655 m in the Salado, a Permian bedded-salt formation. Performance assessment requires a detailed understanding of the response of concentrated brines to both minerals found in the surrounding halite formations as well as nuclear waste, waste packages and the engineered barrier that are emplaced in the repository. Because the primary constituent of the containers used to emplace waste in the repository is steel, there will be substantial quantities of iron available in the repository, which could interact with any brine present.

The WIPP geochemistry model is based on the Pitzer model for the thermodynamics of concentrated electrolyte solutions (Pitzer, 1991). While Pitzer model parameters are available for many of the chemical species in the repository, including both common brine constituents such as Na^+, Mg^{2+}, Ca^{2+}, K^+, HCO_3^-, SO_4^{2-} and Cl^-, as well as the relevant radionuclide species present in the repository, additional thermodynamic properties regarding Fe(II) and Pb(II) species will enhance modeling of the long-term performance of the repository. While a wide variety of Fe(III) parameters are available in the literature, they are not by themselves relevant to descriptions of the behavior of the WIPP repository, because the environmental conditions are expected to favor the ferrous state for iron (Telander and Westerman, 1993; Telander and Westerman, 1997). Several Fe(II) parameters are available in Pitzer (1991). Additionally Millero et al. (1995) have obtained some parameters by fitting previous studies.

The experiments described in this paper are a part of systematic efforts to obtain relevant thermodynamic parameters for iron and lead which are used for packaging and radiation shielding. The goal is to incorporate these parameters into the WIPP geochemistry model. In this study, we have determined the thermodynamic data of the pure-iron end-member of hibbingite and iron hydroxide from solubility studies. These results should be useful not only to the WIPP, but also to many other areas, as numerous occurrences of hibbingite have been observed as mentioned above. In addition, we have studied the reaction of hibbingite with sodium sulfate brines, which resulted in the formation of green rust(II) sulfate and the generation of hydrogen gas.

2. Experimental methods

2.1. Starting material and brine preparation

Solid starting material preparation and solubility experiments were performed within gloveboxes (VAC and Labconco) that have anoxic control systems. Anoxic conditions were maintained using a source gas of 5% H_2 (balance Ar) and Coy Laboratory Products O_2 catalyst boxes. The oxygen concentration within the glovebox was monitored using a Coy O_2 meter, which routinely read 0 ppm. The glovebox O_2 concentrations were also verified using a Delta-F fuel-cell type O_2 meter (DF-310ε) that indicated O_2 concentrations in the range of 3–10 ppm. All aqueous solutions (or DI water prior to preparing solutions) were sparged with the anoxic-glovebox gas in the glovebox for a minimum of 1 h before adding any ferrous iron compounds.

2.1.1. $Fe_2(OH)_3Cl$(s) study

Solubility experiments on $Fe_2(OH)_3Cl$(s) were conducted in 60 mL serum bottles at 25 °C ± 1.5 °C in the VAC glovebox, in 0.1, 1, 2, 3, 4, and 5 molal (m) NaCl solutions prepared from DI water (18 MΩ cm, Barnstead) and NaCl(s) (Fisher, ACS grade). Additionally 0.05, 0.38, 0.76, 1.14, 1.52, and 1.9 m Na_2SO_4 brines were prepared from DI water and Na_2SO_4(s) (Fisher, ACS grade). Two replicates were prepared for each brine concentration. The ratio of solids to liquid in the reactors was 0.7 g solid/60 mL of brine.

In the undersaturation experiments, the solid starting material was prepared by reacting $FeCl_2$•$4H_2O$(s) (Fisher, ACS grade) with KOH (s) (Fisher, ACS grade). A 50 wt.% KOH solution was prepared and centrifuged to minimize carbonate contamination in the final solid phase. Potassium hydroxide and iron chloride were mixed in a molar ratio of 1.86 in a total of 700 mL of water, for a net chloride concentration of 3.2 mol/L (see Section 2.1 of Remazeilles and Refait, 2008). The solids sat overnight in the liquor and were then repeatedly decanted and washed with DI water over a period of one week. Finally the solids were washed with DI water and filtered on Whatman #40 filter paper.

Oversaturation experiments were also performed to ensure that the $Fe_2(OH)_3Cl$(s) phase is precipitated under the conditions explored here. Two reactors were prepared; in each reactor, 0.5 ± 0.1 g $FeCl_2$•$4H_2O$(s) was dissolved directly into 50 mL of 5 m NaCl brine. Next, 1 m NaOH was added to each bottle until the observed electrode pH reading exceeded 9. This procedure was repeated twice as the pH dropped when solids precipitated out of solution. We believe that these experiments approach equilibrium from supersaturation, as $Fe_2(OH)_3Cl$(s) is precipitated in situ in the brine solutions (Fig. 13, Supplemental).

2.1.2. $Fe(OH)_2$ study

Solubility experiments on $Fe(OH)_2$(s) were conducted in serum bottles at 27 °C ± 1.5 °C in the Labconco glovebox, in 0.04, 0.15, 0.5, 1.22, 3.03, and 5.97 molal (m) NaCl solutions. The in situ temperature of the Labconco glovebox is slightly higher than the VAC glovebox; the only temperature control used was the building heating and cooling. The brines and the starting solid phase were prepared simultaneously by adding NaCl(s) (Fisher) to suspensions of $Fe(OH)_2$(s). The $Fe(OH)_2$ (s) was prepared by mixing 24.9925 g $FeCl_2 \cdot 4H_2O$(s) (126 mmol, Fisher), 10.0590 g NaOH(s) (251 mmol, Fisher), and 500 mL of deoxygenated, deionized water within a Labconco glovebox. After two days of aging, the supernatant was volumetrically replaced twice with deoxygenated, deionized water, permitting determination of the definitive dilution factor for dissolved NaCl. After two dilutions over 2 days, further dilution became impractical due to extremely slow sedimentation of the solid, and the calculated concentration of the dissolved NaCl was 0.036 mol/L. Four days after the second dilution, 50 mL of the well-dispersed suspension was transferred into six 60 mL HDPE serum bottles containing 0, 0.3386, 1.3674, 3.4407, 8.7438, and 17.3288 g NaCl(s).

2.2. Analytical methods

X-ray diffraction patterns of the solid phase before and after the experiment were obtained using a Bruker D8 Advance, with Cu-α radiation and a Solex detector.

For total and ferrous iron concentrations, sub-samples were first filtered with 0.2 μm Pall Aerodisc filters and then preserved in 1 M or

2 M HCl (for Ferrozine analysis) or 5% HNO_3 (for ICP-AES analysis) for iron analysis before removal from the glovebox. All acids used were trace metal grade. Total iron concentrations were measured using a Perkin-Elmer dual-view inductively coupled plasma-atomic emission spectrometer (ICP-AES, Perkin-Elmer DV 3300). Calibration blanks and standards were matched with experimental matrices. The correlation coefficients of calibration curves in all measurements were greater than 0.9995. The detection limit was below 0.06 mg/L. The relative standard deviation (RSD), based on replicate analyses, was less than 1.00%. Ferrous (and total) iron concentrations were measured using a Ferrozine method with a Cary 300 UV–VIS spectrometer. The correlation coefficient of the calibration curves from this method was greater than 0.99. The relative standard deviation (RSD), based on replicate analyses, was less than 10%. No significant differences were observed between the Ferrozine and the ICP-AES method.

Chloride concentrations were measured using a Dionex ICS-3000 ion chromatograph using an AS23 anion column, an ASRS300 suppressor, and a Dionex conductivity detector. The correlation coefficient of the calibration curve was greater than 0.999. The RSD of the replicates was less than 15%. For the analysis, the initial chloride concentrations in the brines (determined by the masses of salts and DI water used) were used for the analysis, provided that the chloride analysis results were within 15% of the initial value.

Gas-phase hydrogen concentrations were measured using a C-Squared Inc. hydrogen meter, which measures the thermal conductivity of a sample of gas. The meter was calibrated using lab air and a tank of 5% H_2/balance N_2. Pressure in the serum bottles was measured using a Netech pressure transducer connected to a needle that was used to puncture the septa.

Hydrogen ion concentrations were measured from pH readings using a glass pH electrode. The pH meter and electrode were calibrated using NIST traceable pH buffers (Fisher). Calibrations were performed daily, and calibration checks using one of the buffers above were performed every 2 h. For the $Fe_2(OH)_3Cl(s)$ solubility study, a Mettler–Toledo DG 111-SC Ag/AgCl electrode and a Mettler MA 435 ion analyzer were used. For the $Fe(OH)_2(s)$ solubility study, a Fisher Accumet Semi-Micro Ag/AgCl electrode and a VWR SympHony SP80PI meter were used.

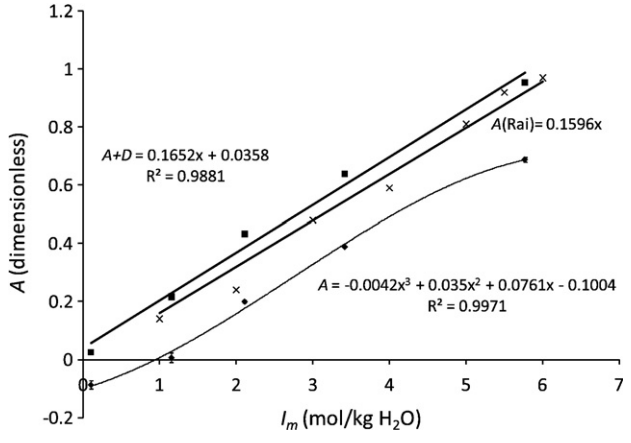

Fig. 1. Correction factor A (dimensionless) versus ionic strength I_m (mol/kg H_2O) and corresponding linear fit for the Mettler–Toledo DG 111-SC Ag/AgCl electrode (blue diamonds and corresponding cubic curve). The squares and corresponding line represent the data and corresponding linear fit for the sum $A+D$, which nearly goes to zero linearly with $I_m \rightarrow 0$, where D is given by Eq. (5). The crosses and corresponding line are the data of Rai et al. (1995); note that Rai et al. (1995) report A = 0.159 I_m, whereas we have found A = 0.1596 I_m from a linear fit of the Rai et al. (1995) data. The source of the discrepancy is unknown.

To compensate for the effect of the junction potential, correction factors for the electrodes were determined by performing Gran titrations on a series of NaCl brines bracketing the brines used in the solubility experiments, as discussed in Rai et al. (1995).

3. Results

3.1. pH electrode correction factors

From Gran titrations of NaCl brines with HCl, an additive correction factor $A(m_{NaCl})$ is determined, which yields the pcH = $-\log_{10}[H^+]$ as a function of the observed pH_{obs},

$$pcH = pH_{obs} + A(m_{NaCl}). \quad (1)$$

For the Mettler–Toledo DG 111-SC Ag/AgCl electrode, the correction factor A was found to be

$$A = -0.1004 + 0.0761 m_{NaCl} + 0.035 m_{NaCl}^2 - 0.0042 m_{NaCl}^3 \quad (2)$$

where m_{NaCl} is the molality of NaCl(aq) (mol/kg water). The pmH = $-\log_{10} m_{H+}$ was determined by converting from molar to molal based on the brine density. A plot of the data and the fit is shown in Fig. 1. For the $Fe_2(OH)_3Cl(s)$ solubility study, we required a cubic fit for the Mettler–Toledo electrode because of the high sensitivity of the log K for this solid phase on the pmH measurements. For the Fisher Accumet Semi-Micro Ag/AgCl electrode, the correction factor A was found to be fit by

$$A = 0.1663 m_{NaCl} - 0.0864, \quad (3)$$

Eq. (3) yields pmH as a function of pH_{obs}. Eqs. (2) and (3) are slightly different than that obtained by Rai et al. (1995) for Orion–Ross electrodes,

$$A_{Rai} = 0.159 m_{NaCl}. \quad (4)$$

The most notable difference between the two equations is that Rai et al. (1995) assumed that the correction factor A goes to zero linearly with m_{NaCl}. However, we did not find this to be the case for our electrodes, as can be seen from Fig. 1. In contrast, it appears to us that at low ionic strengths the correction factor A is dominated by the ion activity coefficient (i.e. the effect of the junction potential becomes subdominant), which implies that $A \sim I_m^{1/2}$ for $I_m \rightarrow 0$. As shown in Fig. 1, when the Debye–Hückel term

$$D = A_\gamma \frac{I_m^{1/2}}{1 + \frac{2}{3} I_m^{1/2}}, \quad (5)$$

where I_m is the molal ionic strength, and $A_\gamma = 0.51001$ is the dimensionless Debye–Hückel parameter, is added to the correction factor A, the sum $A + D$ (with D given by Eq. (5)) closely approaches zero linearly with ionic strength.

3.2. Solubility study of $Fe_2(OH)_3Cl(s)$

3.2.1. XRD of the solid phase

An XRD of the starting material is shown in Fig. 2. The peaks match those of $Fe_2(OH)_3Cl(s)$ (PDF 34-0199). After more than 9 months, XRD (s) of the solids in the 1 m and 5 m reactors were obtained to look for phase changes. These are also shown in Fig. 2. No phase changes are apparent, however the intensity of the peaks increased by a factor of 3 to 10 between the initial solids and the final solids indicating that either amorphous material was present in the solid starting material, or that crystal size increased in solution. An XRD of the 5 m oversaturation experiment is shown in Fig. 13 (Supplemental), taken 10 months after

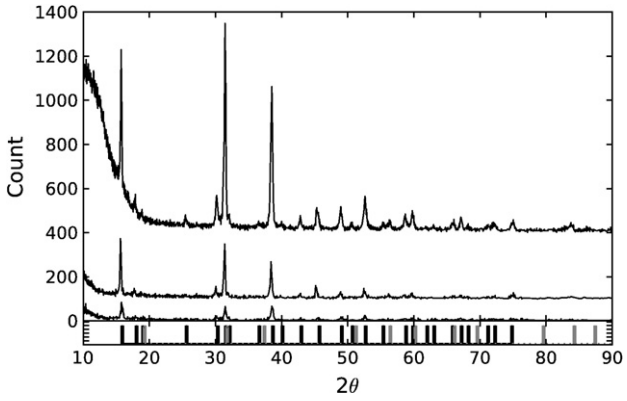

Fig. 2. XRD of the $Fe_2(OH)_3Cl(s)$ starting material (lowermost scan); XRD of solid phase from the 5 m NaCl reactor, removed after 273 days (middle scan); XRD of solid phase from the 1 m NaCl reactor, removed after 344 days (upper scan); XRD reference card data (PDF 34-0199) for $Fe_2(OH)_3Cl(s)$ (lower plot, black lines); XRD reference card data (PDF 13-0089) for $Fe(OH)_2(s)$ (lower plot, grey lines).

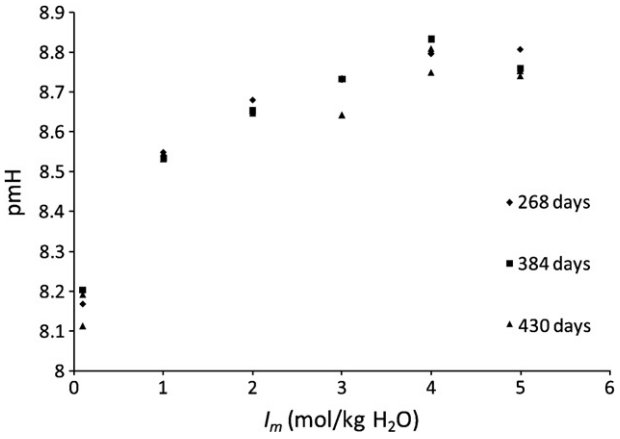

Fig. 4. Negative Log_{10} molal-hydrogen-ion concentration (pmH) versus ionic strength I_m (mol/kg H_2O) of the supporting brine from the undersaturation $Fe_2(OH)_3Cl(s)$ solubility study at different times since the experiment began, as shown in the legend.

the last addition of NaOH to the reactor. Both $Fe_2(OH)_3Cl(s)$ and $Fe(OH)_2$ are present because more base was added than needed to precipitate all of the $Fe_2(OH)_3Cl$.

3.2.2. SEM/EDS of the solid phase

Scanning electron microscopy (SEM) and energy dispersive spectroscopy (EDS) spectra of solid phase removed from the 5 m NaCl reactor are shown in Fig. 14–Fig. 15 (Supplemental). The SEM photo shows a non-descript submicron powder. The EDS spectra confirm the presence of Cl^- in the solid phase.

3.2.3. Aqueous concentrations in NaCl brine

The ferrous iron concentration versus ionic strength for the undersaturation solubility experiments in NaCl brine are shown in Fig. 3 and the pmH is shown in Fig. 4. It appears from the graphs that $m_{Fe^{2+}}$ and pmH had stabilized by no later than 272 days. Oversaturation data was obtained for two reactors in 5 m NaCl brine. These data are discussed in Section 4. Table 1 (Supplemental) gives a list of the data and Fig. 11–Fig. 12 (Supplemental) show $m_{Fe^{2+}}$ and pmH versus time for the various ionic strengths.

3.2.4. Hydrogen production in $NaSO_4$ brines

After several months, we observed that the solid phase in the $NaSO_4$ reactors began darkening, with small bubbles of gas rising upward from the solid phase as shown in Fig. 16 (Supplemental). Eventually the solid phase became a dark green-black color as shown in Fig. 17 (Supplemental). An XRD, shown in Fig. 5, was performed on the solid phase after 167 days. The solid product phase appears to be green rust(II) sulfate, ($Fe^{III}_2Fe^{II}_4(OH)_{12}SO_4(s)$, or $GR(II)SO_4$). After 297 days, the hydrogen concentration was measured in the 0.05 m Na_2SO_4 reactor using a C-Squared hydrogen meter and found to be approximately 15 mol%, three times the hydrogen concentration of the glovebox redox-control gas. The pressure in some bottles after 206 days was found to be as high as 10 psi.

The green rust(II) sulfate was analyzed via scanning electron microscopy and electron dispersion spectroscopy as shown in Fig. 18 (Supplemental). The results were found to be consistent with the formation of green rust(II) sulfate; in particular, the EDS spectrum shows a strong sulfur peak.

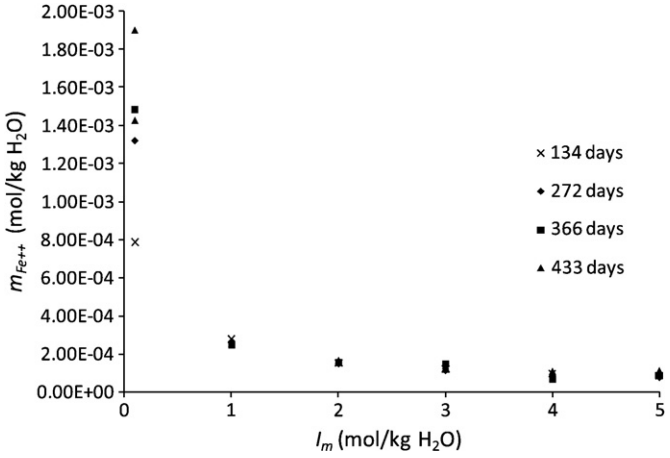

Fig. 3. Ferrous iron concentration m^{2+}_{Fe} (mol/kg H_2O) versus ionic strength I_m (mol/kg H_2O) of the supporting brine from the undersaturation $Fe_2(OH)_3Cl(s)$ solubility study at different times since the experiment began, as shown in the legend. The greatest uncertainty is evident at low ionic strength.

3.3. Solubility study of $Fe(OH)_2$

3.3.1. XRD of the solid phase

Fig. 6 shows the initial solid phase of $Fe(OH)_2(s)$ used in the solubility experiments. No evidence of $Fe_2(OH)_3Cl(s)$ can be seen. Fig. 6 also shows the solid phase after aging in 5.97 m NaCl for 175 days. No phase changes are apparent from the XRD.

3.3.2. Aqueous concentrations in NaCl brine

The ferrous iron concentration for the solubility experiments in NaCl brine are shown in Fig. 7 and the pmH is shown in Fig. 8. It

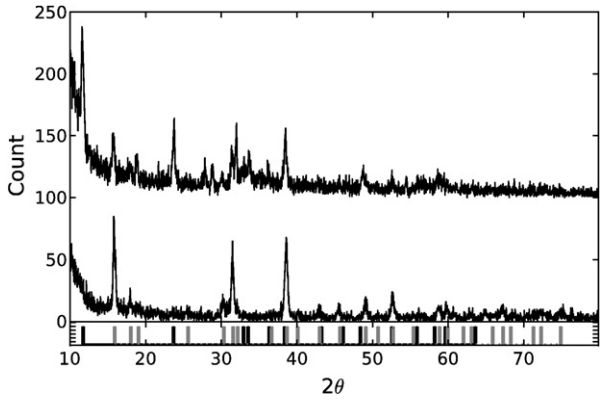

Fig. 5. XRD of solid phase obtained from the 0.76 m Na_2SO_4 reactor (upper scan) after 167 days initially loaded with $Fe_2(OH)_3Cl(s)$; (lower scan); XRD reference card data (PDF 46-0098) for $Fe^{III}_2Fe^{II}_4(OH)_{12}CO_3(s)$ (black lines, lower plot), and $Fe_2(OH)_3Cl(s)$ (grey lines, lower plot).

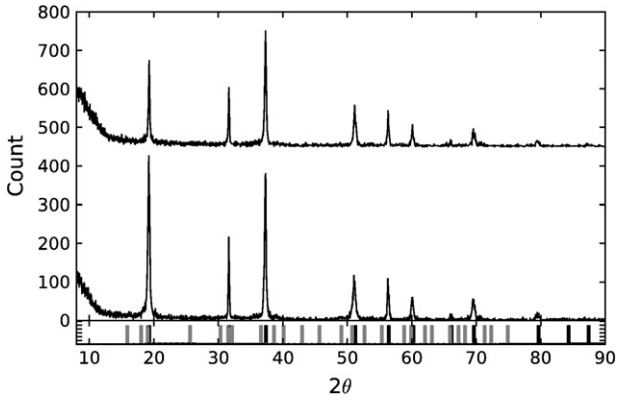

Fig. 6. XRD of initial starting material $Fe(OH)_2(s)$ (lower scan); XRD of $Fe(OH)_2(s)$ aged in 5.97 m NaCl for 175 days (upper scan). $Fe_2Cl(OH)_3(s)$ was not detected however the decrease of $[Fe(II)]_{diss}$, and the increase in pmH, as shown in Fig. 7–Fig. 8, indicates conversion of some $Fe(OH)_2(s)$ to $Fe_2Cl(OH)_3(s)$. XRD reference card data for $Fe(OH)_2$ (s) (lower plot, black lines); XRD reference card data for $Fe_2(OH)_3Cl(s)$ (lower plot, grey lines).

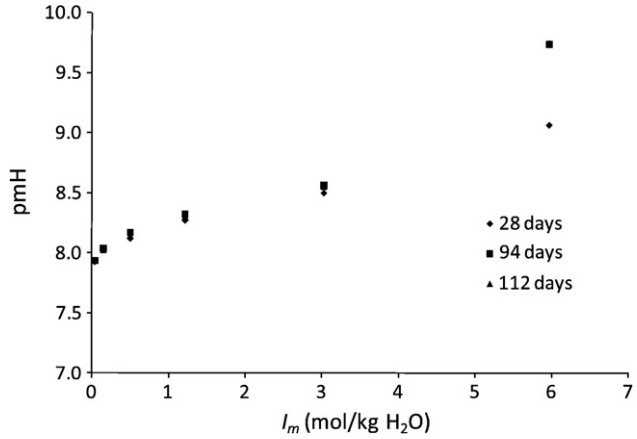

Fig. 8. Negative $\log_{10}$ molal-hydrogen-ion concentration (pmH) versus ionic strength I_m (mol/kg H_2O) of the supporting brine from the $Fe(OH)_2(s)$ solubility study at different times since the experiment began, as shown in the legend.

appears from the graphs that $m_{Fe^{2+}}$ and pmH had stabilized by no later than 94 days.

Between 28 and 112 days, an increase in pH and a corresponding decrease in the concentration of dissolved Fe(II) was observed for the 5.97 m NaCl reactor. We presume that this corresponds to the formation of a small amount of $Fe_2(OH)_3Cl(s)$, although this is not visible from the XRD shown in Fig. 6. Plots of $m_{Fe^{2+}}$ and pmH versus time are shown in Fig. 19–Fig. 20 (Supplemental). The data is also given in Table 2 (Supplemental).

4. Discussion

4.1. $\log_{10} K$ for the dissolution of $Fe_2(OH)_3Cl(s)$ and $Fe(OH)_2(s)$ in NaCl brines, and the Na^+–Fe^{2+} Pitzer interaction coefficient

For the forward dissolution reaction,

$$Fe_2(OH)_3Cl(s) + 3\,H^+ \leftrightarrow 3H_2O + 2Fe^{2+} + Cl^-, \tag{6}$$

we can define the logarithm of the reaction quotient as

$$\log_{10} Q = 2\log_{10} m_{Fe^{2+}} + \log_{10} m_{Cl^-} - 3\log_{10} m_{H^+}, \tag{7}$$

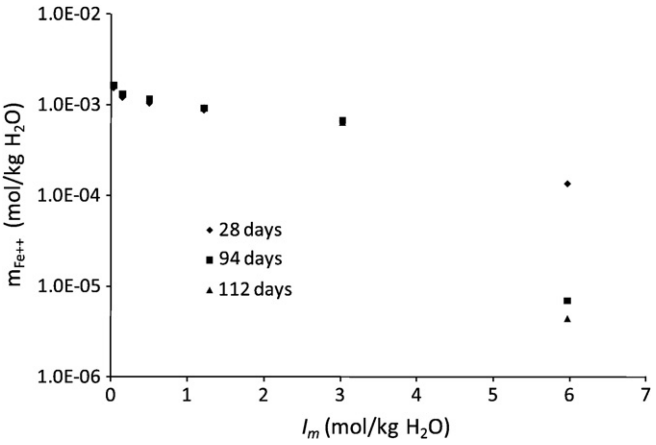

Fig. 7. Ferrous iron concentration m_{Fe}^{2+} (mol/kg H_2O) versus ionic strength I_m (mol/kg H_2O) of the supporting brine from the $Fe(OH)_2(s)$ solubility study at different times since the experiment began, as shown in the legend.

where $m_{Fe^{2+}}$, m_{Cl^-}, and m_{H^+} are the molal concentrations of Fe^{2+}, Cl^-, and H^+, respectively. Fig. 9 plots $\log_{10}Q - 6D + 3\log_{10} a_w$, where a_w is the water activity and D is the Debye–Hückel term given by Eq. (5). Oversaturation data is included in Fig. 9, and shows good agreement with the 5 m NaCl experiments.

For the forward dissolution reaction,

$$Fe(OH)_2(s) + 2\,H^+ \leftrightarrow Fe^{2+} + 2H_2O, \tag{8}$$

the reaction quotient is given by

$$\log_{10} Q = \log_{10} m_{Fe^{2+}} - 2\log_{10} m_{H^+}. \tag{9}$$

Fig. 10 plots $\log_{10} Q - 2D + 2\log_{10} a_w$, where a_w is the water activity and D is the Debye–Hückel term given in Eq. (5).

To determine $\log_{10} K$ for reactions (6) and (8), the speciation code EQ3NR (Wolery and Jarek, 2003) was run for each ionic strength using the measured iron concentration and the initial chloride concentration. The square of the difference between the calculated ($\log_{10} Q_{EQ3NR}$) and measured ($\log_{10} Q_{Exp}$) logarithmic reaction quotient

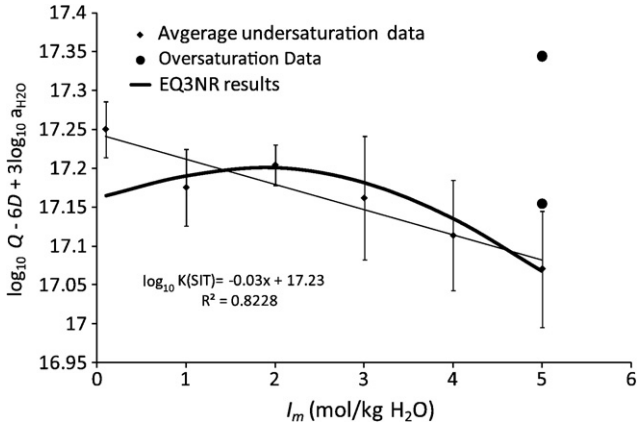

Fig. 9. Plot of $\log_{10} Q$ (reaction quotient) after including the water activity and removing the Debye–Hückel term (Eq. (5)) versus the ionic strength I_m (mol/kg H_2O) for the $Fe_2(OH)_3Cl(s)$ solubility study; both undersaturation (diamonds) and oversaturation (circles) are shown here. EQ3NR modeling results are shown by the curved thick line. The $\log_{10} K$ extrapolated to zero ionic strength by a linear fit (SIT model) through the data is 17.23 (black straight line). The $\log_{10} K$ obtained from EQ3NR runs is 17.12, whether or not $FeOH^+(aq)$ is included in the model.

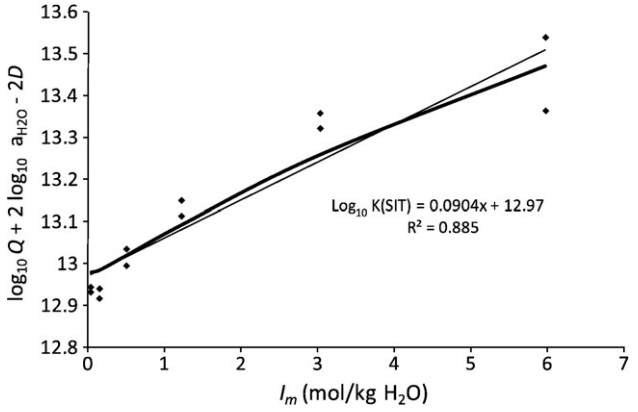

Fig. 10. Plot of $\log_{10} Q$ (reaction quotient) after including the water activity and removing the Debye Hückel term (Eq. (5)) versus the ionic strength I_m (mol/kg H_2O) for the $Fe(OH)_2$(s) solubility study from experimental data (diamonds), and the EQ3NR runs (solid thick line) using a $\log_{10} K = 12.95$. The $\log_{10} K$ extrapolated to zero ionic strength by a linear fit (SIT model) through the data is 12.97 (black straight line).

values for each reactor was summed to determine the objective function,

$$S(x) = \sum_i \left[\log_{10} Q_{EQ3NR}(x) - \log_{10} Q_{Exp}\right]^2, \quad (10)$$

where $x = (\log_{10} K_{Fe_2(OH)_3Cl}\ \log_{10} K_{Fe(OH)_2},\ \theta_{Na^+/Fe^{2+}})$ defines the three parameters to be optimized (the two solubility products and the Na^+–Fe^{2+} interaction Pitzer parameter).

Using a downhill simplex algorithm the value of x that minimizes $S(x)$ was determined. This was achieved by using a Python script that wrapped around EQ3/6. An approximate confidence interval for x was determined by finding solutions x' that satisfy the ellipsoidal constraint

$$S(x') \le S(x)\left[1 + \frac{p}{n-p} F(p, n-p, \alpha)\right], \quad (11)$$

where $F(p,n-p,\alpha)$ is the F distribution for p parameters, n data points, and a 100α% confidence interval (Draper and Smith, 1998). With $p = 1$, Eq. (11) is equivalent to Student's t-test (see Section 1.5 of Draper and Smith, 1998); it should be noted that Eq. (11) is only truly valid for a linear least-squares problem. Our use of this statistic is equivalent to linearizing the problem around the solution point x. At the 95% confidence interval we obtained $\log_{10} K = 17.12 \pm 0.15$ for $Fe_2(OH)_3Cl$(s), $\log_{10} K = 12.95 \pm 0.13$ for $Fe(OH)_2$(s), and $\theta_{Na^+/Fe^{2+}} = 0.08 \pm 0.03$. In obtaining these results we have used all of the undersaturation $Fe_2(OH)_3Cl$(s) data listed in Table 1 (Supplemental) and the 94 and 112 day $Fe(OH)_2$(s) data from Table 2 (Supplemental).

Only two iron species, Fe^{2+} and $FeOH^+$, were included in the model. The Pitzer parameter for Fe^{2+}–Cl^- was taken from Pitzer (1991). Iron(II) chloride complexes are not considered in our modeling, as the specific interaction between Fe^{2+} and Cl^- absorbs the effect of complex formation in the Pitzer model. When the Pitzer interaction parameters of $MgOH^+$–Cl^- are assigned to $FeOH^+$–Cl^- as analogs, the results are unchanged to the significant figures reported herein. The results also did not depend on whether the $FeOH^+$ complex was included in the model. Thus, for the results reported herein, the $FeOH^+$–Cl^- interaction has an insignificant and negligible effect on modeling results. The experimental data and modeling results shown in Figs. 9 and 10 demonstrate that the Fe^{2+}–Cl^- and Fe^{2+}–Na^+ Pitzer parameters adequately capture the behavior of this system.

As a check, $\log_{10} K$ was also computed using the specific ion interaction theory (SIT, Biedemann et al., 1982; Grenthe et al., 1997) model, which is obtained as the intercept of the straight line in Figs. 9 and 10, yielding $\log_{10} K_{Fe_2(OH)_3Cl} = 17.23$ and $\log_{10} K_{Fe(OH)_2} = 12.97$ respectively. Given the differences in the formulations of the SIT and Pitzer models, the agreement in the values of the $\log_{10} K$ is excellent. Additionally, for $Fe(OH)_2$(s), the $\log_{10} K = 12.95 \pm 0.13$ corresponds to a $\log_{10} K_{sp}$ of -15.05 ± 0.13. This value is in good agreement with the solubility product of crystalline $Fe(OH)_2$(s) of −15.1 listed in the NIST database (Smith and Martell, 2004). It is reasonable to compare solubility products obtained from Pitzer modeling to SIT and the NIST database for low-charge species (Guillaumont et al., 2003).

4.2. Gibbs free energy of hibbingite

Given our estimate for $\log_{10} K$ for the dissolution of hibbingite, we are also able to calculate a Gibbs free energy of formation for hibbingite, and compare it to other values reported in the literature. Remazeilles and Refait (2008) estimated $\Delta_f G$ of $Fe_2(OH)_3Cl$(s) as −923.5 kJ mol^{-1}. Based on $\Delta_f G_{H_2O(l)} = -237.18$ kJ mol^{-1}, $\Delta_f G_{Cl^-} = -131.2$ kJ mol^{-1} adopted by Remazeilles and Refait (2008), and $\Delta_f G_{Fe^{2+}} = -91.5$ kJ mol^{-1} adopted by Refait et al. (1999), the logarithmic equilibrium constant for reaction (6) would be 17.91. This value is about 0.7 log units higher than the value obtained from our modeling calculations, which indicates that pure-iron end-member of hibbingite is more stable than previously thought. In this study, we derived a value of $\Delta_f G = -928.0 \pm 0.9$ (using the confidence interval on $\log_{10} K$) kJ mol^{-1} for the pure-iron end-member of hibbingite. In order to compare directly with the value of Remazeilles and Refait (2008), our presented value of $\Delta_f G$ is derived from the Gibbs free energy of formations ($\Delta_f G_{H_2O(l)}$, $\Delta_f G_{Cl^-}$ and $\Delta_f G_{Fe^{2+}}$) listed above.

4.3. Production of hydrogen by $Fe_2(OH)_3Cl$ in sulfate brines

For the reaction of $Fe_2(OH)_3Cl$(s) in Na_2SO_4 brines we consider that the reaction

$$3Fe_2(OH)_3Cl(s) + SO_4^{2-} + OH^- + 2H_2O(l) \leftrightarrow Fe_6(OH)_{12}SO_4(s) + 3Cl^- + H_2(g) \quad (12)$$

may adequately describe the redox reaction that appears to be occurring; we have not performed sufficient analyses to verify the stoichiometry of reaction (12). A similar reaction has been observed previously under anoxic conditions by Bessiere et al. (1999):

$$5Fe(OH)_2(s) + FeSO_4(aq) + 2H_2O \leftrightarrow Fe_6(OH)_{12}SO_4 + H_2(g), \quad (13)$$

and by Kulkarni (2006) for zero-valent iron. The conversion of GR(II) SO_4 to magnetite has also been observed under anoxic conditions (Sumoondur et al., 2008a,b), which implies that the presence of Na_2SO_4 acts as a catalyst for the final production of magnetite in Na_2SO_4-bearing brines.

5. Applications to nuclear waste isolation

When low-carbon steel waste containers in geological repositories are partially corroded as Fe-hibbingite in chloride-rich brine, the assemblage of the remaining metallic iron and Fe-hibbingite is likely to buffer the oxygen fugacity in the repository:

$$Fe_2(OH)_3Cl(s) \leftrightarrow 2Fe(s) + O_2(g) + H^+ + Cl^- + H_2O(l). \quad (14)$$

Based on the equilibrium constant of Fe-hibbingite determined in this study, in combination with thermodynamic data from the NBS thermodynamic table (Wagman et al., 1982) for the reaction

$$Fe(s) + 0.5O_2(g) + 2H^+ \leftrightarrow Fe^{2+} + H_2O(l), \quad (15)$$

which has a $\log_{10} K = 55.37$, the log f_{O_2} buffered by the above assemblage is –85 at pH 9, $a_{H_2O} = 0.75$, and $a_{Cl^-} = 5$ m. Therefore,

the assemblage of metallic iron and Fe-hibbingite would provide a reducing environment. A reducing environment is favorable to the performance of the geological repository by maintaining actinides important to the WIPP performance assessment (PA) in a reduced oxidation state, which reduces their mobility.

6. Summary

Using solubility measurements, we have determined the logarithm of the equilibrium constant of Fe-hibbingite to be 17.12 ± 0.15. This value is about 0.7 log units lower than the value determined by Remazeilles and Refait (2008), and suggests that Fe-hibbingite may be more stable than indicated by the log K determined in the earlier study. The assemblage of metallic iron and Fe-hibbingite in mildly alkaline and chloride-rich brines would buffer the geological repository under reducing conditions similar to that buffered by the assemblage of metallic iron and $Fe(OH)_2(s)$. We hope that our thermodynamic data for the pure-iron end-member of hibbingite will provide valuable insight into its stability in various geological environments, including deep geological repositories for nuclear waste in salt formations.

Acknowledgements

The authors would like to thank Shelly Johnsen, Terry MacDonald, Raul Rascon, and Leslie Kirkes for their valuable help in performing the lab work that went into this manuscript. We thank Dr. Karen Johannesson and another journal reviewer for their detailed and insightful reviews, and Dr. Jeremy Fein for his editorial efforts. Their reviews and efforts have substantially improved our presentation.

Appendix A. Supplementary data

Supplementary data to this article can be found online at doi:10.1016/j.chemgeo.2010.10.003.

References

Anthony, J.W., Bideaux, R.A., Bladh, K.W., Nichols, M.C., 2003. Handbook of Mineralogy, 3. Mineralogical Society of America, Chantilly, VA.

Bessiere, J., Perdicakis, M., Humbert, B., 1999. Formation of sulfated green rust II $Fe_6(OH)_{12}SO_4$ by oxidation of ferrous sulfate by water. Series II: ChimieComptes Rendus de l'Academie des Sciences 2 (2), 101–105.

Biedemann, G., et al., 1982. Modeling the Migration of Lanthanides and Actinides in Ground Water; the medium dependence of equilibrium constants. In: Lutz, W. (Ed.), Scientific basis for nuclear waste management V: Materials Research Society Symposium Proceedings, pp. 791–800.

Buchwald, V.F., Koch, C.B., 1995. Hibbingite (β-Fe2(OH)3Cl), a chlorine-rich corrosion product in meteorites and ancient iron objects. Meteoritics 30 (5), 493-493.

Cawthorn, R.G., Luvimbe, C., Slabbert, M., 2009. Suspected presence of hibbingite in olivine pyroxenites adjacent to the UG2 chromitite, Bushveld Complex, South Africa. Canadian Mineralogist 47, 1075–1085.

Draper, N.R., Smith, H., 1998. Applied Regression Analysis. Wiley Series in Probability and Mathematical Statistics. John Wiley & Sons, Inc, New York.

Grenthe, I., Plyasunov, A.V., Spahiu, K., 1997. Estimations of medium effects on thermodynamic data. In: Grenthe, I., Puigdo Menech, I. (Eds.), Modeling in Aquatic Chemistry. French Nuclear Energy Agency, Organization for Economic Co-Operation and Development, Paris, France, pp. 325–426.

Guillaumont, R., et al., 2003. Update on the Chemical Thermodynamics of Uranium, Neptunium, Plutonium, Americium, and Technetium. Elsevier, Amsterdam, The Netherlands. 919 pp.

Kulkarni, D.V., 2006. Electrochemical Deposition of Green Rust on Zero-Valent Iron. Texas A&M, Austin. 61 pp.

Lee, M.R., Bland, P.A., 2004. Mechanisms of weathering of meteorites recovered from hot and cold deserts and the formation of phyllosilicates. Geochimica et Cosmochimica Acta 68 (4), 893–916.

Millero, F.J., Yao, W., Aicher, J., 1995. The speciation of Fe(II) and Fe(III) in natural waters. Marine Chemistry 50, 21–39.

Oswald, H.R., Feitknecht, W., 1964. Über die Hydroxidhalogenide $Me_2(OH)_3Cl$, -Br, -J zweiwertiget Metalle (Me = Mg, Ni, Co, Cu, Fe, Mn). Helvetica Chimica Acta 47 (1), 272–289.

Pitzer, K.S., 1991. Activity Coefficients in Electrolyte Solutions. CRC Press, Boca Raton, FL.

Rai, D., Felmy, A.R., Juracich, S.P., Rao, F., 1995. Estimating the hydrogen ion concentration in concentrated NaCl and Na_2SO_4 electrolytes. SAND94-1949, Sandia National Laboratories, Albuquerque, NM. .

Refait, P., et al., 1999. Chemical composition and Gibbs standard free energy of formation of Fe(II)–Fe(III) hydroxysulphate green rust and Fe(II) hydroxide. Clay Minerals 34 (3), 499–510.

Reguer, S., Neff, D., Bellot-Gurlet, L., Dillmann, P., 2007. Deterioration of iron archaeological artefacts: micro-Raman investigation on Cl-containing corrosion products. Journal of Raman Spectroscopy 38 (4), 389–397.

Remazeilles, C., Refait, P., 2008. Formation, fast oxidation and thermodynamic data of Fe (II) hydroxychlorides. Corrosion Science 50, 856–864.

Saini-Eidukat, B., Kucha, H., Keppler, H., 1994. Hibbingite, γ-Fe2(OH)3Cl, a new mineral from the Duluth Complex, Minnesota, with implications for oxidation of iron-bearing compounds and transport of metals. American Mineralogist 79 (5–6), 555–561.

Saini-Eidukat, B., Rudashevsky, N.S., Polozov, A.G., 1998. Evidence for hibbingite–kempite solid solution. Mineralogical Magazine 62 (2), 251–255.

Smith, R.M., Martell, A.E., 2004. NIST critical selected stability constants of metal complexes database version 8.0 for Windows. NIST Standard Reference Database 46, National Institute of Standards and Technology, Gaithersburg, MD. .

Springer, G., 1989. Chlorine-bearing and other uncommon minerals in the Strathcona deep copper zone, Sudbury district, Ontario. Canadian Mineralogist 27, 311–313.

Sumoondur, A., Shaw, S., Ahmed, I., Benning, L.G., 2008a. Green rust as a precursor for magnetite: an in situ synchrotron based study. Mineralogical Magazine 72 (1), 201–204.

Sumoondur, A., Shaw, S., Ahmed, I., Benning, L.G., 2008b. Green rust is a precursor to magnetite: direct evidence from an in situ diffraction study. Geochimica et Cosmochimica Acta 72 (12), A913–A.

Telander, M.R., Westerman, R.E., 1993. Hydrogen Generation by Metal Corrosion in Simulated Waste Isolation Pilot Plan Environments: Progress Report for the Period November 1989 through December 1992. SAND92-7347, Pacific Northwest Laboratory, Richland, WA.

Telander, M.R., Westerman, R.E., 1997. Hydrogen Generation by Metal Corrosion in Simulated Waste Isolation Pilot Plant Environments. SAND96-2538, Batelle Pacific Northwest Laboratory, Richland, WA.

Wagman, D.D., et al., 1982. The NBS tables of chemical thermodynamic properties: selected values for inorganic and C_1 and C_2 organic substances in SI units. Journal of Physical and Chemical Reference Data 11 (Supplement No. 2).

Wolery, T.J., Jarek, R.L., 2003. Software User's Manual, EQ36, Version 8.0. Sandia National Laboratories, Albuquerque, NM.

Appendix A. Experimentally Measured Concentrations

Table 1. Experimental measurements from the $Fe_2(OH)_3Cl(s)$ solubility study. The undersaturation sample ID's below are given by XX-Cl-Fe(OH)2-YY, where XX = 0.1, 1, .., 5 is the ionic strength of the brine I_m (mol H_2O) , and YY is the replicate = 1 or 2. The oversaturation sample ID's below are given by 5m-Cl-Fe(OH)2-O-YY, where YY is the replicate = 1,2. The sample ID is a unique identified for each reactor; multiple measurements from the same sample ID appear in the table for different measurement times. For the undersaturation experiment, time was measured from the day that the solids and brine were combined. For the oversaturation experiments, time was measured from the date of the last addition of NaOH. Note that pH measurements and sampling for iron analysis were not necessarily on the same day and could differ by as much as 16 days as shown below.

ID	mFe^{2+} (mol/kg H_2O)	pmH	mCl^- (mol/kg H_2O)	Days after Experiment began (pmH measurement)	Days after experiment began (mFe^{2+} measurement)
0.1-Cl-Fe(OH)2-2	1.3E-03	8.17	0.10	268	272
0.1-Cl-Fe(OH)2-1	1.5E-03	8.20	0.10	384	366
0.1-Cl-Fe(OH)2-1	1.4E-03	8.19	0.10	433	430
0.1-Cl-Fe(OH)2-2	1.9E-03	8.11	0.10	433	430
1-Cl-Fe(OH)2-2	2.7E-04	8.55	1.00	268	272
1-Cl-Fe(OH)2-1	2.5E-04	8.53	1.00	384	366
1-Cl-Fe(OH)2-1	2.6E-04	8.55	1.00	433	430
1-Cl-Fe(OH)2-2	2.6E-04	8.53	1.00	433	430
2-Cl-Fe(OH)2-2	1.5E-04	8.68	2.00	268	272
2-Cl-Fe(OH)2-1	1.6E-04	8.65	2.00	384	366
2-Cl-Fe(OH)2-1	1.7E-04	8.65	2.00	433	430
2-Cl-Fe(OH)2-2	1.7E-04	8.65	2.00	433	430
3-Cl-Fe(OH)2-2	1.2E-04	8.73	3.00	268	272
3-Cl-Fe(OH)2-1	1.5E-04	8.73	3.00	384	366
3-Cl-Fe(OH)2-1	1.2E-04	8.73	3.00	433	430
3-Cl-Fe(OH)2-2	1.4E-04	8.64	3.00	433	430

4-Cl-Fe(OH)2-2	8.8E-05	8.80	4.00	268	272
4-Cl-Fe(OH)2-1	6.9E-05	8.83	4.00	384	366
4-Cl-Fe(OH)2-1	7.8E-05	8.81	4.00	433	430
4-Cl-Fe(OH)2-2	1.1E-04	8.75	4.00	433	430
5-Cl-Fe(OH)2-2	7.8E-05	8.81	5.00	268	272
5-Cl-Fe(OH)2-1	8.9E-05	8.76	5.00	384	366
5-Cl-Fe(OH)2-1	1.1E-04	8.74	5.00	433	430
5-Cl-Fe(OH)2-2	9.1E-05	8.75	5.00	433	430
5m-Cl-Fe(OH)2-O-1	8.64E-06	9.52	5.00	41	45
5m-Cl-Fe(OH)2-O-2	7.42E-06	9.50	5.00	41	45
5m-Cl-Fe(OH)2-O-1	6.56E-06	9.55	5.00	157	139
5m-Cl-Fe(OH)2-O-2	7.68E-06	9.51	5.00	157	139
5m-Cl-Fe(OH)2-O-1	6.95E-06	9.54	5.00	203	206
5m-Cl-Fe(OH)2-O-2	8.21E-06	9.56	5.00	203	206
5m-Cl-Fe(OH)2-O-1	9.46E-06	9.49	5.00	557	557
5m-Cl-Fe(OH)2-O-2	5.92E-06	9.53	5.00	557	557

Table 2. Experimental measurements from the $Fe(OH)_2(s)$ solubility study. Here the sample ID's are unique identifiers but do not convey information on the system being studied. We refer the reader to the table for the conditions of each sample.

Sample ID	mFe^{2+} (mol/kg H_2O)	pmH	mCl^- (mol/kg H_2O)	Days after experiment began
SQDLTN+0	1.52E-03	7.924	0.04	28
SQDLTN+1	1.19E-03	8.035	0.15	28
SQDLTN+2	1.03E-03	8.118	0.50	28
SQDLTN+3	8.66E-04	8.267	1.22	28
SQDLTN+4	6.54E-04	8.494	3.03	28
SQDLTN+5	1.33E-04	9.059	5.97	28
SQDLTN+0	1.63E-03	7.94	0.04	94
SQDLTN+1	1.31E-03	8.04	0.15	94
SQDLTN+2	1.15E-03	8.17	0.50	94
SQDLTN+3	9.20E-04	8.32	1.22	94
SQDLTN+4	6.68E-04	8.56	3.03	94
SQDLTN+5	6.90E-06	9.74	5.97	94
SQDLTN+0	1.64E-03	7.94	0.04	112
SQDLTN+1	1.30E-03	8.03	0.15	112
SQDLTN+2	1.16E-03	8.15	0.50	112
SQDLTN+3	9.23E-04	8.30	1.22	112
SQDLTN+4	6.38E-04	8.55	3.03	112
SQDLTN+5	4.38E-06	9.75	5.97	112

Appendix B. pH electrode correction factors

Table 3. pH electrode correction factors, *A*, versus I_m (mol/kg H_2O) for the Mettler-Toledo DG 111-SC Ag/AgCl electrode.

I_m (mol/kg H_2O)	*A* (dimensionless)	Standard Deviation in *A* (dimensionless)
0.1035	-0.08665	0.014513432
1.155569	0.00677	0.016122055
2.111162	0.199944	0.004379196
3.418392	0.389014	NA
5.76837	0.687368	0.008165106

Table 4. pH electrode correction factors, *A*, versus I_m (mol/kg H_2O) for the Fisher Acumet Semi-Micro Ag/AgCl electrode.

I_m (mol/kg H_2O)	*A* (dimensionless)
0.0305	-0.043
0.334	-0.040
1.01	0.058
3.01	0.395
6.015	0.918
6.015	0.923

Appendix C. Supplemental Information

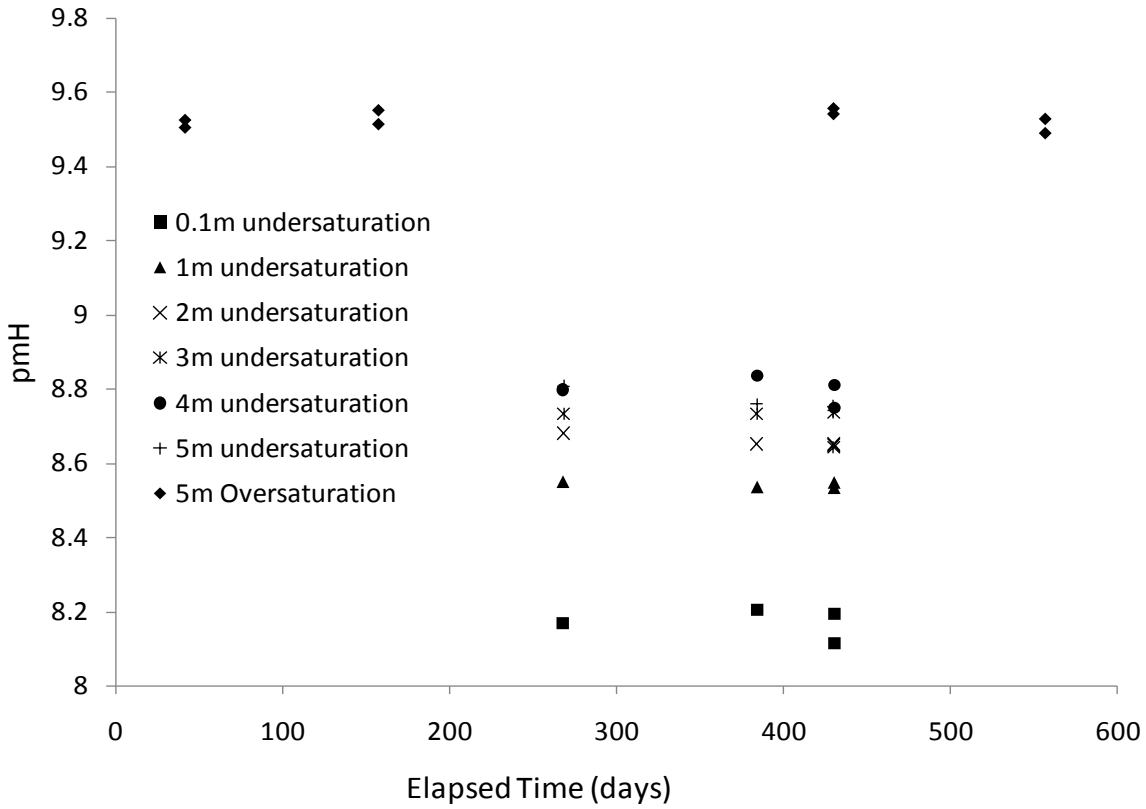

Figure 1. Log_{10} molal-hydrogen-ion concentration (pmH) versus time (days) from the $Fe_2(OH)_3Cl(s)$ solubility study. Note that in the oversaturation experiment, an excess of base was added hence the pmH is about 0.5 units above that of the undersaturation experiments.

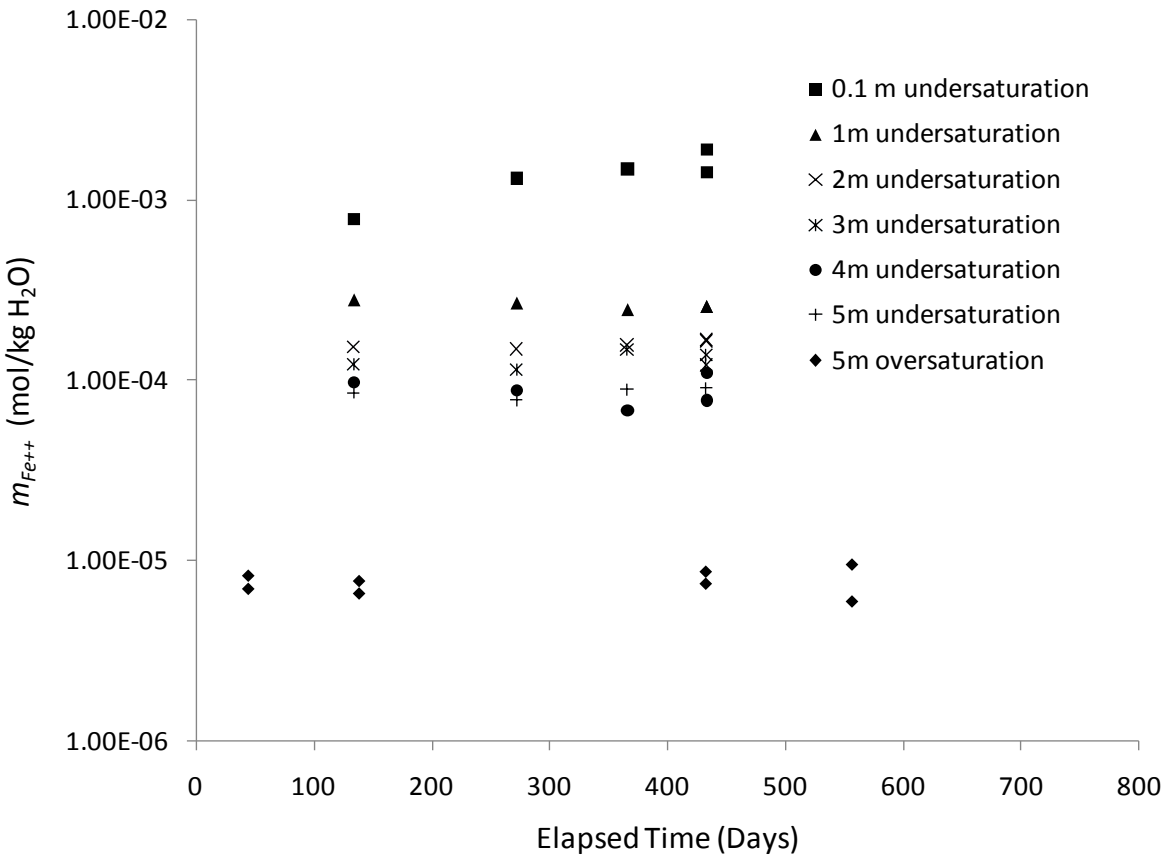

Figure 2. Ferrous iron concentration m_{Fe++} (mol/kg H_2O) versus time (days) from the $Fe_2(OH)_3Cl$(s) solubility study. Note that in the oversaturation experiment, an excess of base was added hence m_{Fe++} is about one order of magnitude below that of the undersaturation experiments.

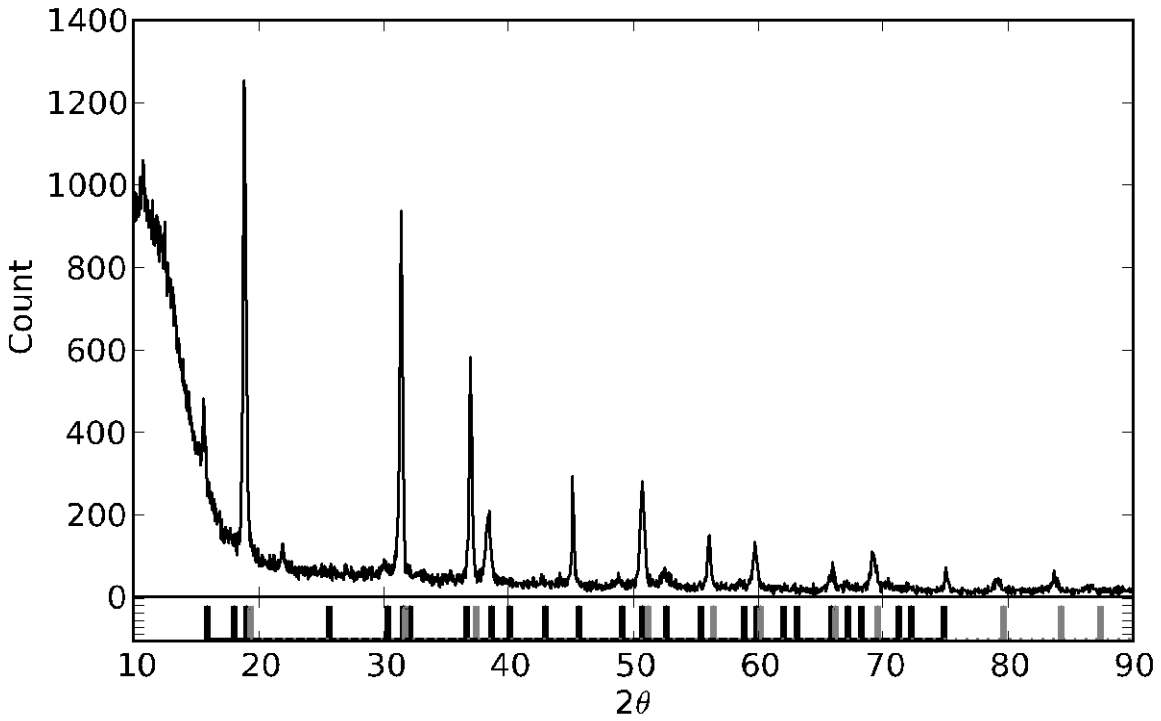

Figure 3. XRD of solid phase from the 5m NaCl oversaturation reactor, removed after 311 days; XRD reference card data (PDF 34-0199) for $Fe_2(OH)_3Cl(s)$ (lower plot, black lines); XRD reference card data (PDF 13-0089) for $Fe(OH)_2(s)$ (lower plot, grey lines). This reactor is a mixture of $Fe_2(OH)_3Cl(s)$ and $Fe(OH)_2(s)$ owing to the fact that an excess of base was added.

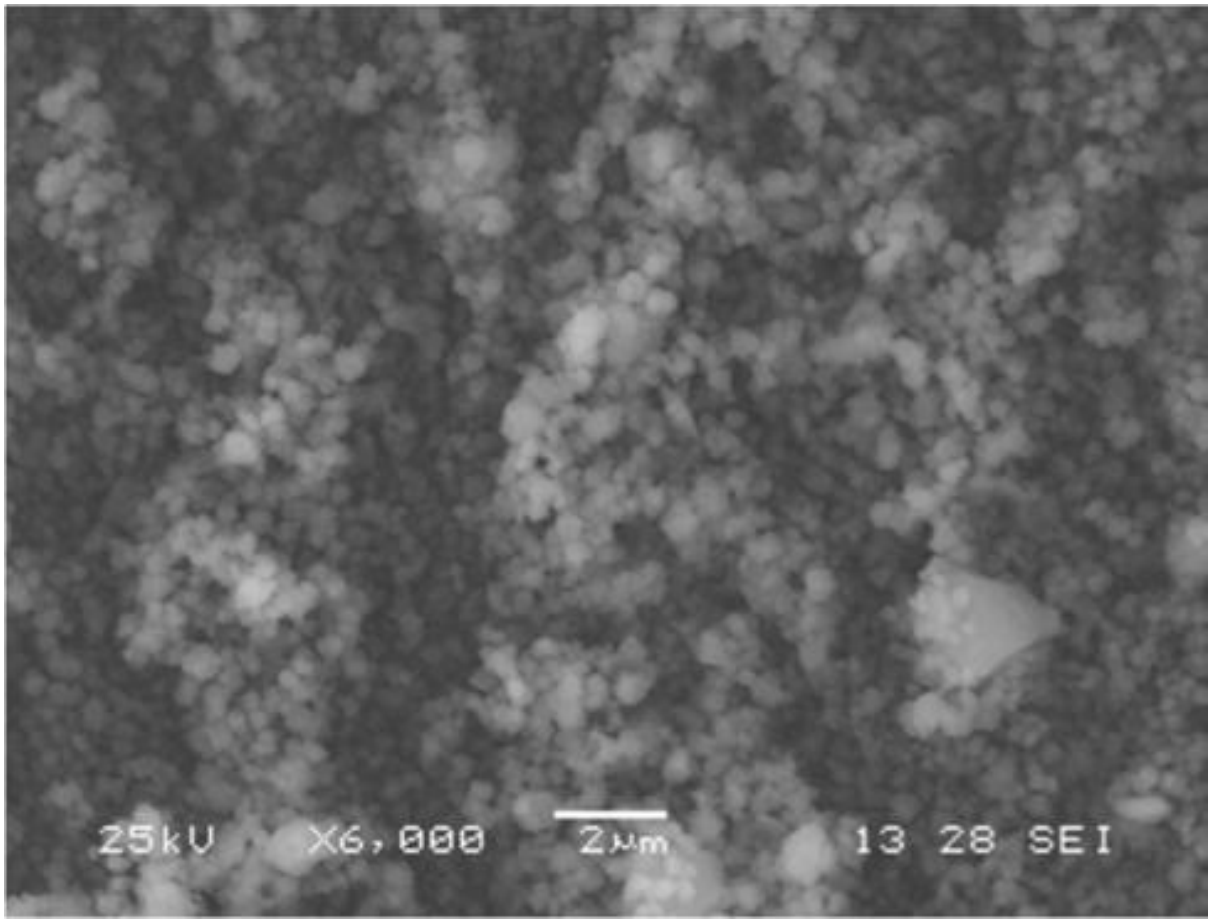

Figure 4. SEM image of $Fe_2(OH)_3Cl$(s) removed from the 5m NaCl brine reactor.

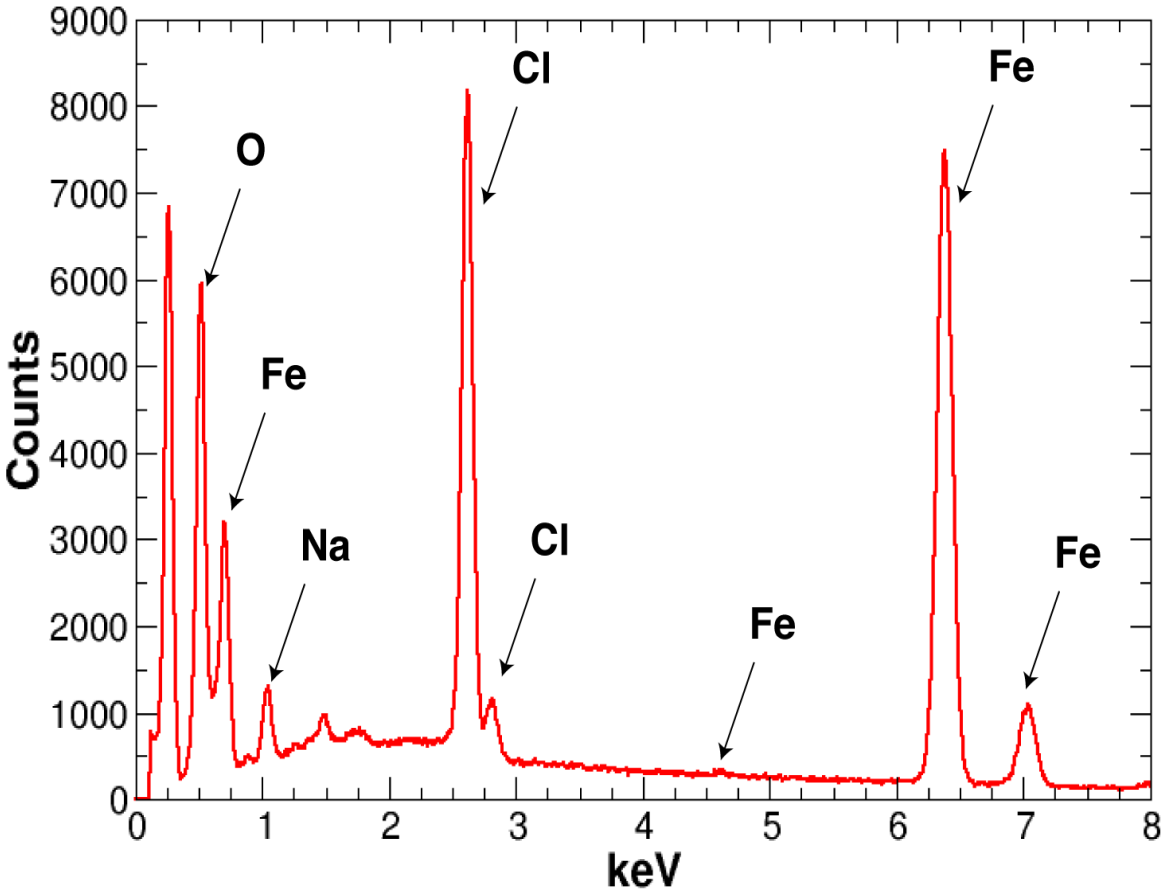

Figure 5. EDS spectra of the $Fe_2(OH)_3Cl$(s) material shown in Figure 5**Error! Reference source not found.**. The large peak to the left of oxygen is carbon (from the carbon tape) and the detector window (beryllium).

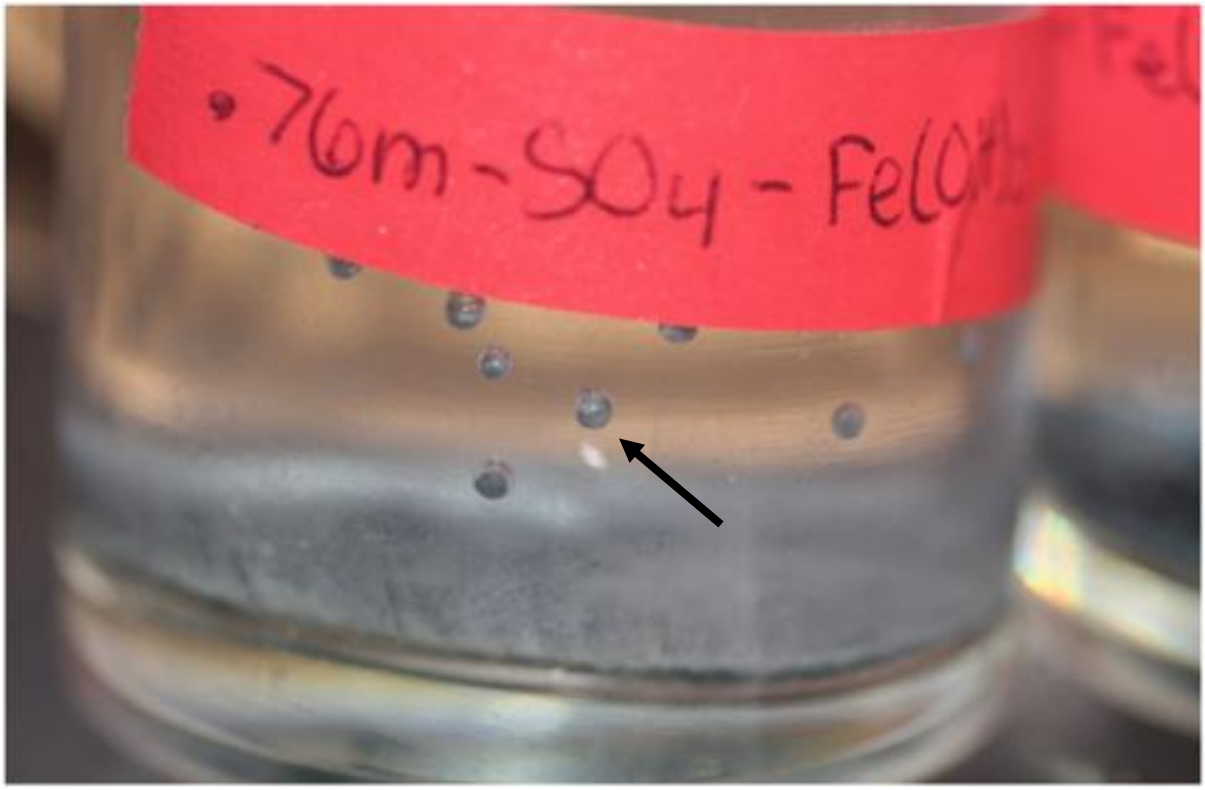

Figure 6. A 0.76 m Na_2SO_4 reactor containing a starting material of $Fe_2(OH)_3Cl$(s) at 171 days. Bubbles (black arrow) could be seen rising from the solid phase throughout the experiment.

Figure 7. Green rust in the 0.05 m Na_2SO_4 reactor after 171 days.

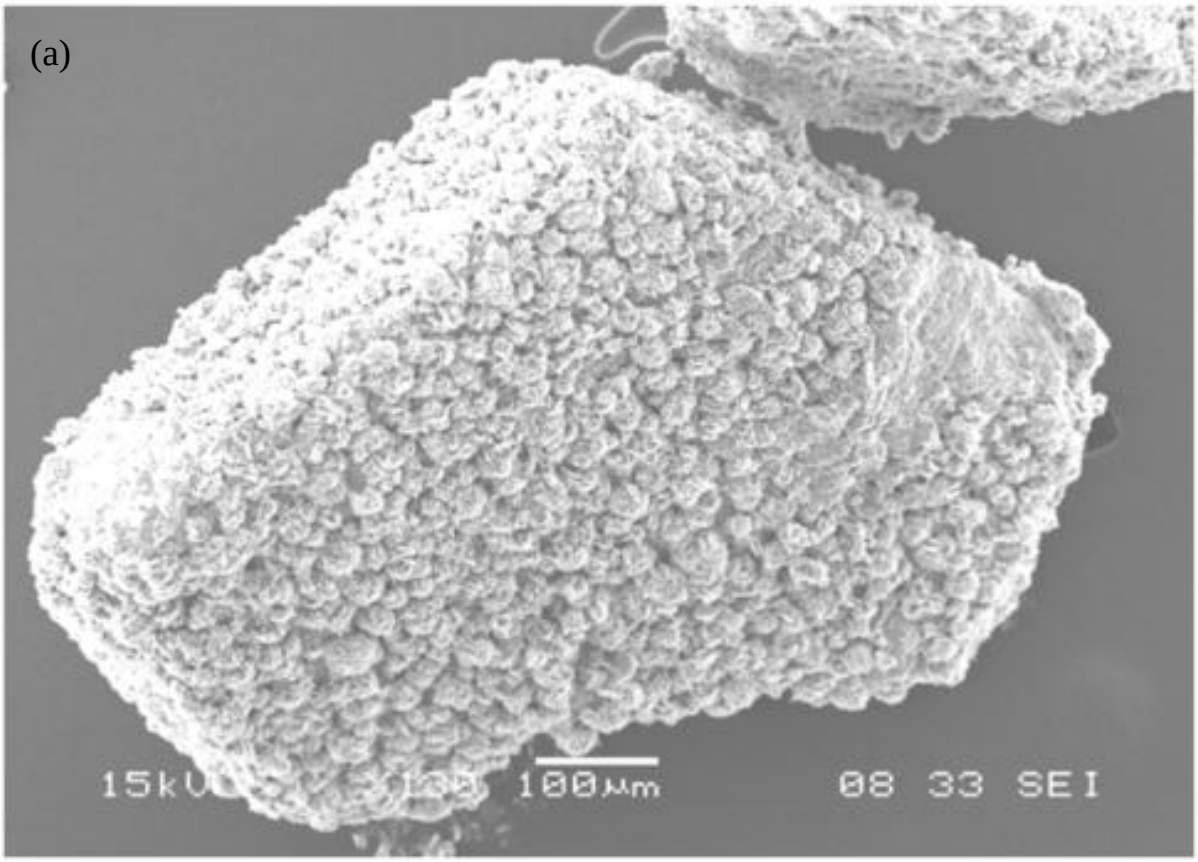

66

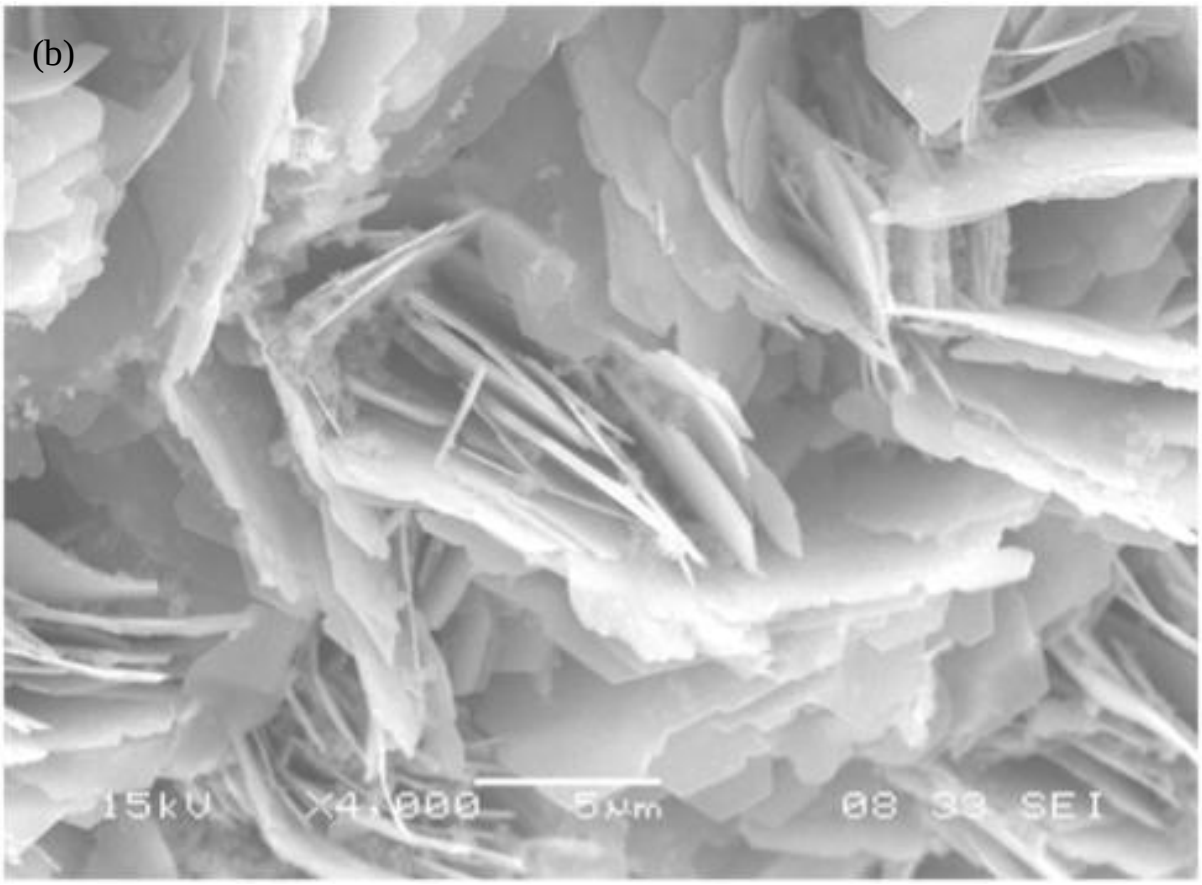

67

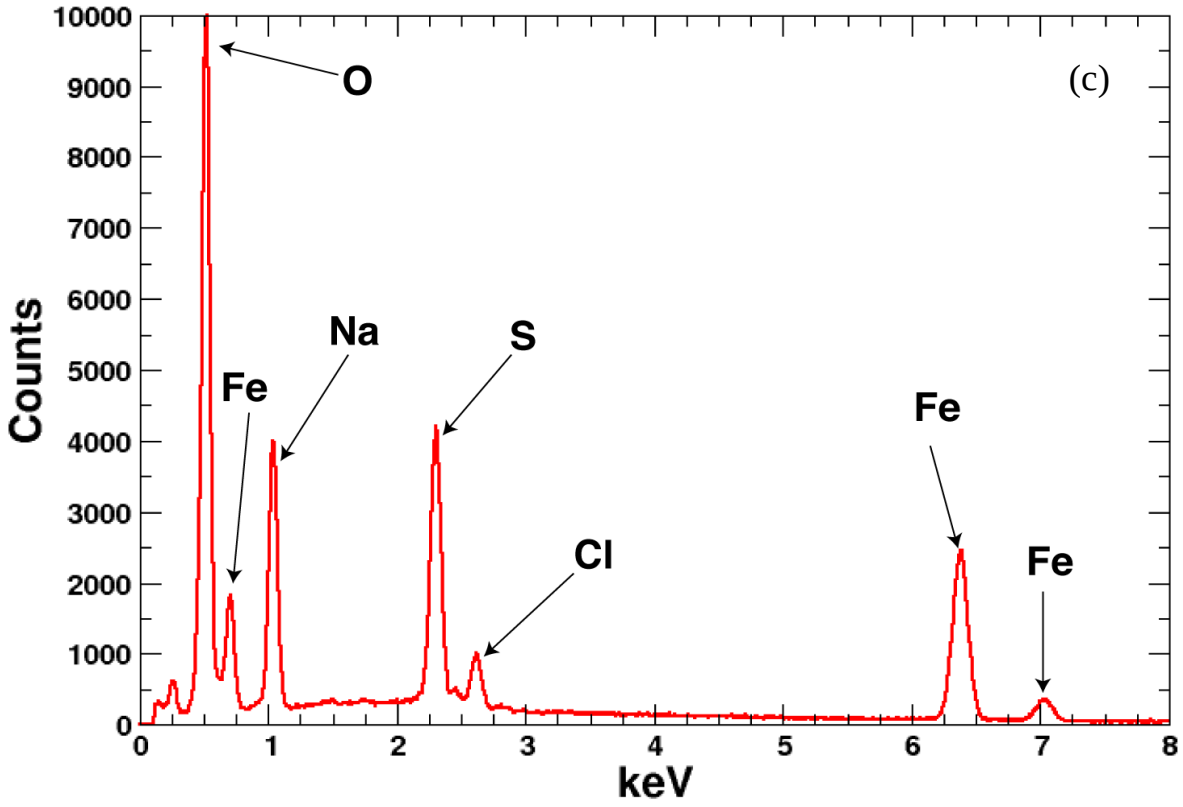

Figure 8. (a) & (b) SEM images and (c) associated EDS spectra of GR(II)SO_4 solid phase produced in the Na_2SO_4 reactor.

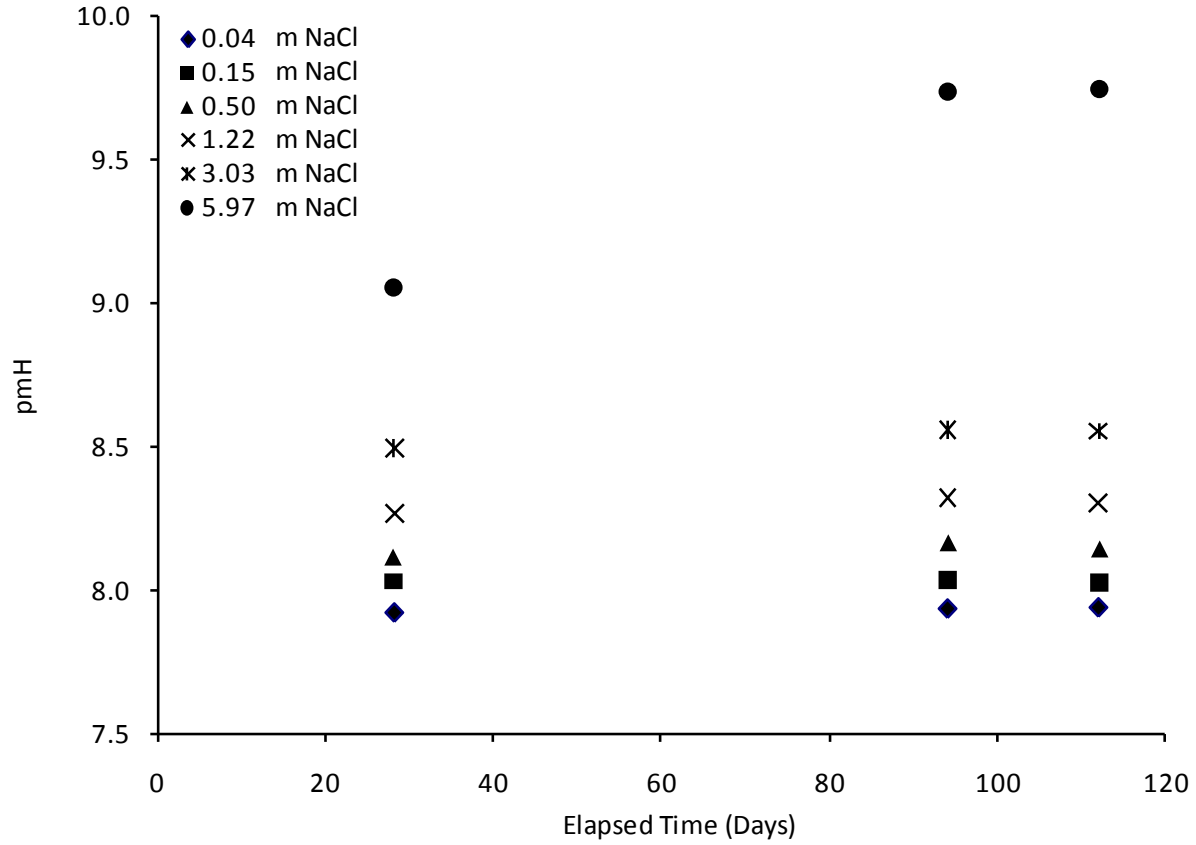

73

74 Figure 9. Log_{10} molal-hydrogen-ion concentration (pmH) versus time (days) from the
75 $Fe(OH)_2(s)$ solubility study.

76

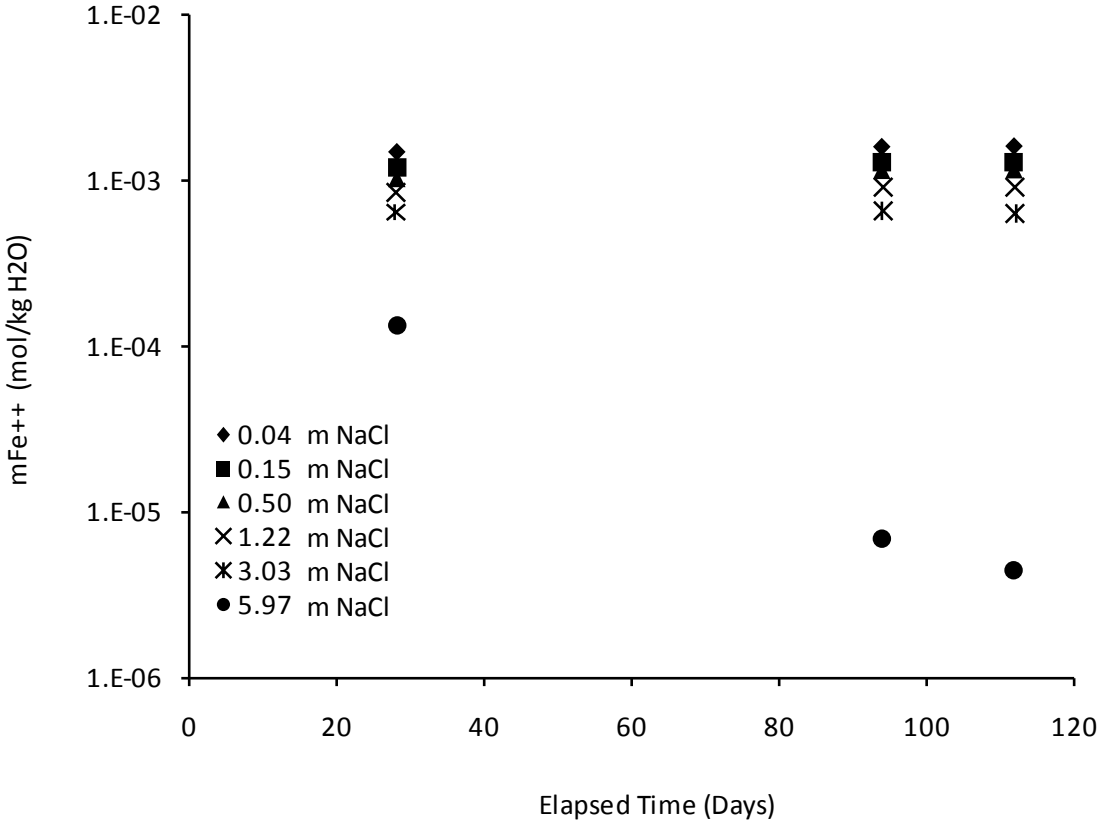

77

78 Figure 10. Ferrous iron concentration $m_{Fe^{++}}$ (mol/kg H_2O) versus time (days) from the
79 $Fe(OH)_2(s)$ solubility study.

80